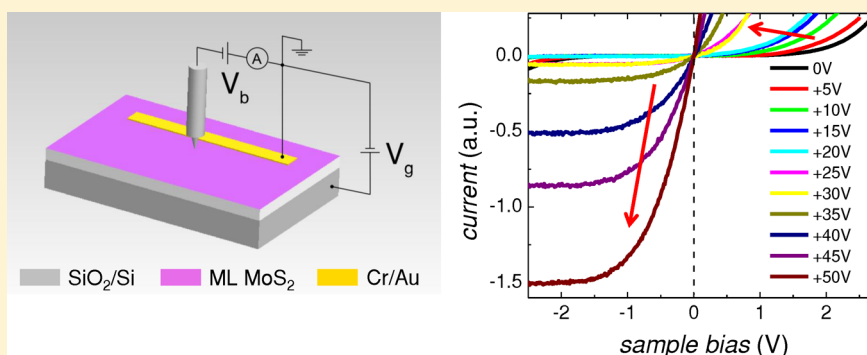


Atomic-Scale Spectroscopy of Gated Monolayer MoS₂Xiaodong Zhou,[†] Kibum Kang,[§] Saien Xie,[§] Ali Dadgar,[†] Nicholas R. Monahan,[‡] X.-Y. Zhu,[‡] Jiwoong Park,[§] and Abhay N. Pasupathy[†][†]Department of Physics and [‡]Department of Chemistry, Columbia University, New York, New York 10027, United States[§]Department of Chemistry and Chemical Biology, Cornell University, Ithaca, New York 14853, United States

Supporting Information



ABSTRACT: The electronic properties of semiconducting monolayer transition-metal dichalcogenides can be tuned by electrostatic gate potentials. Here we report gate-tunable imaging and spectroscopy of monolayer MoS₂ by atomic-resolution scanning tunneling microscopy/spectroscopy (STM/STS). Our measurements are performed on large-area samples grown by metal–organic chemical vapor deposition (MOCVD) techniques on a silicon oxide substrate. Topographic measurements of defect density indicate a sample quality comparable to single-crystal MoS₂. From gate voltage dependent spectroscopic measurements, we determine that in-gap states exist in or near the MoS₂ film at a density of $1.3 \times 10^{12} \text{ eV}^{-1} \text{ cm}^{-2}$. By combining the single-particle band gap measured by STS with optical measurements, we estimate an exciton binding energy of 230 meV on this substrate, in qualitative agreement with numerical simulation. Grain boundaries are observed in these polycrystalline samples, which are seen to not have strong electronic signatures in STM imaging.

KEYWORDS: Monolayer molybdenum disulfide, scanning tunneling microscopy/spectroscopy, single-particle band gap, exciton binding energy, grain boundary

Monolayer MoS₂ is a semiconducting transition metal dichalcogenide (TMD) with unique electronic^{1–5} and optical^{2,3,6–8} properties. A unique feature of monolayer semiconducting TMDs is the tunability of their properties by the electrostatic environment. By using an appropriate substrate or electrostatic gate, it is possible to strongly influence the dielectric screening and carrier concentration in the TMD. Appropriate substrate and gate engineering can thus modify fundamental transport and optical properties such as the electrical conductance,^{1,9–11} excitonic properties,^{8,12,13} band gap,¹⁴ electron–phonon coupling,¹⁵ and even structure^{16,17} of the TMD. These effects have been probed to date chiefly by transport measurements in a field-effect transistor (FET) geometry^{1,9–11} as well as by optical measurements on gated substrates.^{6–8,12–14} To complement these transport and optical measurements, it is desirable to directly probe the single-particle electronic structure of these new materials as a function of field-effect doping. In the past, several single-particle spectroscopic probes such as angle-resolved photoemission^{18,19} and scanning tunneling microscopy (STM)^{20–25} have been used to probe the electronic structure of monolayer TMD.

Because of reasons of sample cleanliness and difficulty in making Ohmic contact²⁶ with the TMD film, these studies have so far been confined to studying monolayer TMD films placed or grown on metallic or semimetallic substrates, with successful gate-dependent STM measurements only being achieved on multilayer films.²⁷ Such gate-dependent STM studies on graphene have provided important information on sample homogeneity,^{28,29} scattering mechanisms,²⁸ electron–electron³⁰ and electron–phonon³¹ interactions, and insights into new electronic phenomena at the atomic scale.^{32,33} It is thus highly desirable to achieve gate-dependent spectroscopic measurements on monolayer TMD films.

In the present work, we describe methods by which the typical problems of cleanliness and contact resistance can be overcome, allowing us to perform high-quality spectroscopic measurements on gated monolayer MoS₂. Key to our new measurements is the availability of a new class of monolayer

Received: February 2, 2016

Revised: April 7, 2016

Published: April 11, 2016

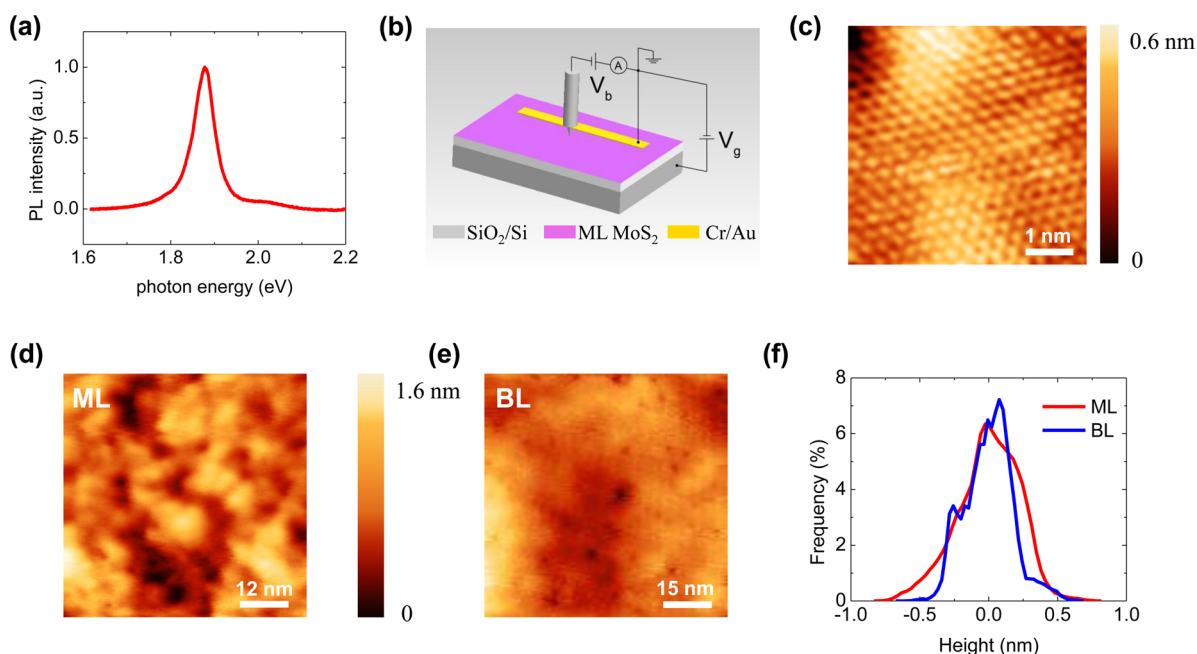


Figure 1. (a) PL spectra of monolayer MoS₂ displaying a prominent peak at 1.87 eV. (b) Schematic of the STM measurement setup. An electrostatic gate voltage is applied to the monolayer MoS₂ through a SiO₂/Si substrate during the STM/STS characterization. (c) Atomic resolution STM image of monolayer MoS₂ showing a triangular atomic lattice of S with lattice constant of 3.2 Å (set point: $V = 2$ V, $I = 40$ pA). (d, e) Large-area STM images of monolayer (ML) and bilayer (BL) MoS₂ (set point for ML, $V = 2.5$ V, $I = 20$ pA; set point for BL, $V = 2.5$ V, $I = 20$ pA). (f) Histograms of the topographic height distributions for (d) ML and (e) BL MoS₂.

MoS₂ samples. The initial experimental work on monolayer MoS₂ was performed on micron-sized samples produced by mechanical exfoliation.² While such samples can be produced cleanly on an insulating substrate without the use of lithography or polymers, the small size of these samples gives rise to large contact resistances to metal electrodes. More recently, chemical vapor deposition (CVD) has been used to grow large-area films of MoS₂, which enables statistically relevant experimental studies as well as applications.^{34–36} These growth techniques use solid precursors, which lead to contamination from unreacted species on the surface and make STM imaging difficult. Very recently, a fully vapor-based precursor approach has been used to create extremely uniform, high-quality films of monolayer MoS₂ over the wafer scale.³⁷ This newly developed, metal–organic chemical vapor deposition (MOCVD) technique is a major advance in the large-scale growth of monolayer TMD films with spatial homogeneity and high electrical performance in spite of its polycrystalline structure. Importantly for STM measurements, the use of only vapor precursors leads to a much cleaner surface than other CVD techniques. Additionally, the wafer scale continuity of the sample implies that making the contact area large enough can minimize the resistance to a drain contact as demonstrated by a recent transport study showing that a large contact area helps to realize full carrier injection.³⁸ Because of the new availability of these MOCVD films, we are able to perform high-resolution STM imaging and spectroscopy on the film under influence of a back-gate electrode for the first time.

Our experiments begin by the growth of monolayer MoS₂ samples directly on a SiO₂/Si substrate,³⁷ which optimizes the growth time to produce films that have near-complete coverage over the entire 4-in. wafer. The thickness of the film is primarily monolayer (>95%), with occasional small patches (micron-sized) of bilayer or thicker regions. The MoS₂ films are first characterized using optical absorption, photoluminescence

(PL), and Raman spectroscopy. Our monolayer films show PL spectra with peak position at 1.87 eV that are similar to previous reports on exfoliated and CVD samples (Figure 1a).^{2,3} After characterization, our substrates are cleaved into pieces that are 2 mm × 10 mm in size. To perform STM, we deposit a metal electrode that serves as the drain of the tunneling current. To minimize contact resistance to the MoS₂ film, we deposit a Cr/Au (2/50 nm) electrode of dimensions 50 μm × 3 mm on the MoS₂ film. The electrode is deposited by evaporation through a stencil mask to preserve the cleanliness of the MoS₂ film. The MoS₂ film is introduced into the ultrahigh vacuum preparation chamber and annealed at 150 °C for several hours to remove surface contamination before the STM measurement. Our measurements indicate that the quality of the film is not affected by annealing at temperatures below 300 °C. The sample is then loaded into the STM and measurements performed without additional sample preparation. To further overcome the contact issue of monolayer MoS₂, we perform all of the measurements in this letter at room temperature to minimize the effect of the Schottky barrier between the metal electrode and MoS₂ film that becomes a severe problem at cryogenic temperatures. Figure 1, panel b shows the schematic of our device setup. During the STM measurements, the electrode in contact with the film is kept grounded. To independently tune the carrier concentration in the MoS₂ film, the Si wafer is biased with a gate voltage V_g that is tuned in the range of ±50 V. STM measurements are performed with a W tip that is biased at a potential V_b with respect to the sample.

Figure 1, panel c is an atomic resolution STM image of monolayer MoS₂. It clearly reveals a hexagonal atomic lattice as expected from the top sulfur layer with the appropriate lattice constant of 3.2 Å. Figure 1, panel d is the STM topography of a typical 60 × 60 nm² area of monolayer MoS₂. The sample surface shows a root-mean-square (RMS) roughness of 225 pm with the lateral size scale of the roughness being a few nm.

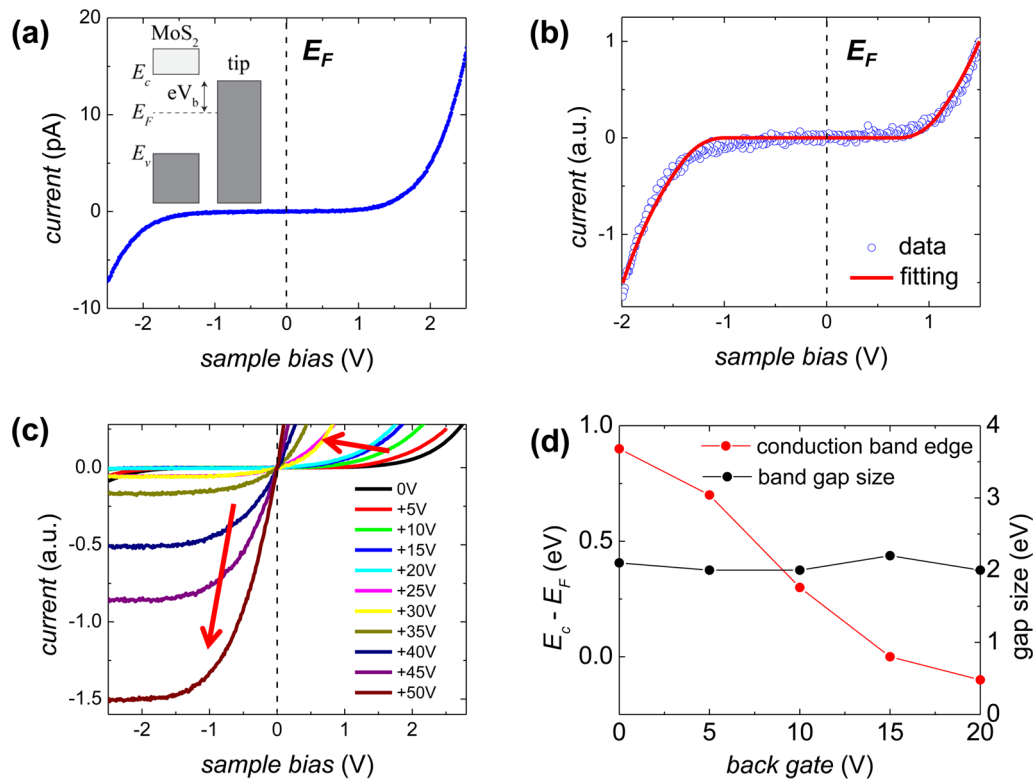


Figure 2. Evolution of electronic spectrum $I(V)$ with back gate V_g . (a) $I(V)$ spectrum taken at $V_g = 0$ V showing a tunneling gap of 2.1 eV. A band alignment diagram is shown in the inset (set point: $V = 2.8$ V, $I = 25$ pA). (b) A fit to the $I(V)$ curve in panel a using Bardeen's formula. (c) A series of $I(V)$ spectra taken at different back gate V_g from 0 to +50 V. The set point bias V varies from 1 to 2.8 V, and current I varies from 10 pA to 30 pA for different back gate voltages. The conduction band edge E_c is moving toward the Fermi level E_F with increasing back gate voltages as denoted by the red arrows. (d) The position of the conduction band edge E_c and the extracted band gap as a function of back gate V_g .

While height contrast in an STM image can come both from topographic roughness as well as density of states variations, we note that the roughness of monolayer MoS₂ that we measure is comparable to the roughness of monolayer graphene on SiO₂, a sample with very different density of states variations. Both of these numbers are also comparable to the intrinsic roughness of the SiO₂ substrate itself, indicating that monolayer MoS₂ conforms well to the SiO₂ surface and the height variations we measure are primarily topographic. We occasionally find and measure bilayer MoS₂ patches in our sample (see [Supporting Information](#)). In contrast to the large-scale topography of monolayer MoS₂, we find that bilayer MoS₂ ([Figure 1e](#)) displays a much smoother topography on the large scale, with a typical RMS roughness of 174 pm. [Figure 1](#), panel f displays the histograms of the height distribution for monolayer and bilayer MoS₂, illustrating this difference. We can understand the reduced roughness of bilayer MoS₂ as due to the increase in bending stiffness of MoS₂ with thickness. Similar effects in roughness have been reported on graphene before by STM.³⁹ This layer thickness-dependent roughness can potentially be used to determine the van der Waals interaction between individual sheets of MoS₂, though appropriate theoretical models are currently lacking for this.

To measure the electronic spectrum of monolayer MoS₂ with STM, we record the tunneling current I as we sweep the sample bias voltage V_b . We perform this measurement tens of microns away from the metal contact to avoid effects of the Schottky barrier in our measurements. This $I(V)$ measurement can be performed at a fixed value of the back gate voltage V_g . In [Figure 2](#), panel a, we show a typical $I(V)$ spectrum acquired at $V_g = 0$

V. The spectrum clearly shows the presence of a tunneling gap where the current is zero. For this particular spectrum, the tunneling gap extends from -1.2 V to $+0.9$ V, for a total gap of 2.1 V. In [Figure 2](#), panel c, we plot a series of $I(V)$ taken at different back gate voltages from 0 V to +50 V. We see that the application of a positive gate voltage systematically tunes the positive edge of the tunneling gap toward the Fermi level. These observations are completely consistent with the expected spectrum of a two-dimensional (2D) semiconductor that is being electrostatically gated. The tunneling gap measured in the STM is directly related to the semiconductor band gap. We will discuss reasons below why the two are not necessarily identical in magnitude, but in what follows, we will interchangeably use the two notations. The positive edge of the tunneling gap thus corresponds to electron tunneling into the unoccupied conduction band of MoS₂, while the negative edge of the tunneling gap corresponds to hole tunneling into the occupied valence band. The fact that the conduction and valence band edges are roughly equidistant from the Fermi level at zero gate voltage implies that the sample has a compensated hole and electron density as grown. As the gate voltage is increased in the positive direction, the sample becomes capacitively charged with electrons, thus adding electrons into the conduction band. This shifts the edge of the conduction band toward the Fermi level, exactly as observed in [Figure 2](#), panel c.

To extract the size of the band gap as a function of back gate, we can fit the $I(V)$ curve at each value of V_g using Bardeen's formula:⁴⁰

$$I(V) = -\frac{4\pi e}{\hbar} \rho_t \int_{-\infty}^{\infty} \rho_s(\varepsilon) \times T(\varepsilon) (f(\varepsilon - eV) - f(\varepsilon)) d\varepsilon$$

Here ρ_t (ρ_s) is the tip's (sample's) density of state (DOS), d is the tip-sample distance ($\sim 5-8$ Å), Φ is the averaged work function of the W tip and monolayer MoS₂ (~ 5 eV),^{41,42} $f(\varepsilon)$ is the Fermi function at room temperature, and $T(E) \approx e^{-2d/\hbar\sqrt{2m(\Phi - \frac{eV}{2} - E)}}$ is the energy-dependent tunneling matrix element. We assume for our experiment that the energy dependence of the tip DOS is weak. To make a fit to the experimental $I(V)$, we have to assume a functional form to the energy dependence of the sample DOS ρ_s . In the case of MoS₂, multiple electron and hole bands are present near the gap, which can contribute to tunneling.⁴³ Indeed, in previous experiments on other monolayer TMDs, additional features in the experimental spectra have been used to estimate the contributions of different bands to tunneling.⁴⁴ In our case, we do not see such additional features clearly at room temperature. Thus, we use a simple one-band approximation of the semiconductor DOS, where parabolic bands have an energy-independent $\rho_s = \frac{m^*}{\pi\hbar^2}$. We also allow the conduction and valence bands to have different effective mass m^* and hence different DOS. Thus, we model the experimental spectrum by the following ρ_s :

$$\rho_s(E) = \begin{cases} \rho_0 & E < -E_v \\ 0 & -E_v < E < E_C \\ \alpha\rho_0 & E > E_C \end{cases}$$

We use this function to fit to the experimental spectrum. We limit our fit to the bias range close to the edge of the gap (< 500 mV) where the one-band approximation is reasonable. We note that our results for the band gap are reasonably independent (10–20 meV) of the precise functional form of the DOS assumed outside the gap. In our fit, the magnitude of the parameter ρ_v, ρ_0 that enters the tunneling current is fixed by the normalization condition of the tunnel junction. We thus have three free parameters that determine the spectrum: the positions of the valence and conduction band edges E_v and E_C , and the ratio of the DOS of the conduction band to the valence band α . Shown in Figure 2, panel b is a typical example of a fit to the $I(V)$ curve shown in Figure 2, panel a. The fitted conduction band edge E_C is 0.9 eV, and the valence band edge E_v is -1.2 eV, giving a band gap $\Delta = E_C - E_v = 2.1$ eV. The conduction band edge E_C is seen to move toward the Fermi level with increasing gate voltage indicating electron doping of the MoS₂ sheet. We can perform similar fits to the $I(V)$ curves at each value of $V_g < 25$ V. At larger gate voltages, the Fermi level reaches the edge of the conduction band, and the spectrum near the Fermi level is dominated by defect states, making the fitting routine unreliable. Additionally, the valence band edge moves out of the range of safe voltages we can apply. In Figure 2, panel d, we plot the band gap and the position of the conduction band edge E_C as a function of the back gate voltage for $V_g < 25$ V. The fits show that within our measurement accuracy (about 50 meV), the band gap extracted is independent of gate voltage.

We first discuss the shift of E_C (or equivalently the shift of E_F) as a function of the back gates as plotted in Figure 2, panel d. Given the capacitance per unit area between the gate and the MoS₂ sheet $C = 1.28 \times 10^{-8}$ F cm⁻² ($C = \varepsilon_0\varepsilon_r/d$; $\varepsilon_r = 3.9$; $d = 270$ nm), one estimates that the MoS₂ sample will be charged

with electrons at a rate of 8×10^{10} V⁻¹ cm⁻², shifting the Fermi level E_F into the conduction band. The rate at which the Fermi level shifts, $\kappa = dE_F/dV_g$, depends on multiple factors. The first factor is the presence of thermally activated intrinsic carriers $n = Ne^{-\Delta/kT}$. Here, N is the number of carriers in the valence bands of monolayer MoS₂ ($\sim 10^{15}$ /cm²). At room temperature, the number of such thermally excited carriers ($\sim 10^{-19}$ /cm²) is still negligible given the large band gap of MoS₂, and we can thus neglect this effect. The second effect that determines κ is the density of states of the conduction band n_c . In the absence of intrinsic or extrinsic carriers, the Fermi level will be located close to the midpoint of the semiconducting gap. Upon adding electron carriers, the Fermi level should immediately jump to the edge of the conduction band. Once it enters the conducting band, the Fermi level will shift at a rate given by $\kappa = \frac{C}{en_c}$.

Experimentally, we do not see an abrupt jump from the midpoint of the gap to the edge of the conduction band as a function of applied gate voltage. Instead, the Fermi level E_F shifts gradually to the conduction band (see Figure 2c) as the back gate V_g is increased from 0 to +20 V. This indicates the presence of in-gap states that can be filled by the gate bias. These in-gap states are created by the defects or trapped charge in or near MoS₂. We see experimentally that the shift of the Fermi level is fairly linear with V_g in the gap, indicating that the in-gap states are distributed uniformly in energy within the gap. We apply a linear fit to $E_F(V_g)$ from 0 to +20 V (gap region) to extract the shift rate. The experimental shift rate $\kappa = 0.062$ eV/volt within the gap corresponds to a defect density $n_D = 1.3 \times 10^{12}$ eV⁻¹ cm⁻². We note that the charge traps can be located either in the MoS₂ itself or in the underlying SiO₂.

We next turn to the measured tunneling gap in scanning tunneling spectroscopy (STS) spectra. The tunneling gap clearly originates from the band gap of MoS₂. However, two important effects should be considered before one can make quantitative comparisons between the tunneling gap and the band gap. The first of these is the local doping caused by the STM tip itself, typically called tip-induced band bending (TIBB) in the context of three-dimensional (3D) semiconductors. TIBB in general will make the tunneling gap appear larger than the band gap of the semiconductor, with detailed magnitudes depending on the electrostatics of the junction.^{45–47} The second effect is the screening of the tunneling electron in the MoS₂ by the dielectric environment, commonly referred to as the image potential effect.^{48,49} This effect will make the tunneling gap appear smaller than the true band gap. In STM measurements on 3D semiconductors, TIBB can be a large fraction of a volt due to the poor screening in the semiconductor. Our situation is different for two reasons. First, our electrostatic geometry is significantly different due to the presence of the gate electrode. We find that the calculated magnitude of TIBB is smaller than that usually seen in prior measurements on 3D semiconductors due to the screening from the back gate electrode. Second, a significant amount of lateral tunneling is present inside the MoS₂ film that reduces the effect of the TIBB in the tunneling spectrum. Our estimate for the overestimation of the band gap due to TIBB is roughly 140 ± 50 meV (details in the Supporting Information). Coincidentally, the estimate of the image potential (also provided in the Supporting Information) is roughly of the same magnitude. Since the two effects have opposite sign, they cancel each other, implying that the observed tunneling gap is equal to

the single-particle band gap of MoS₂ (to within 50 meV due to uncertainties in the tip shape).

We can use the STS estimate of the band gap (2.1 eV) in conjunction with the PL measurements (1.87 eV) on monolayer MoS₂ to estimate the exciton binding energy in our samples. This calculation results in an estimate of 230 ± 50 meV for the exciton binding energy. This large exciton binding energy is a consequence of the strong Coulomb interactions due to lower dimensionality and reduced dielectric screening of monolayer MoS₂.^{50,51} Interestingly, our measured band gap on SiO₂ is very similar to previous measurements of monolayer MoS₂ on graphite²⁰ indicating the screening effects of the two substrates on the band gap is very similar. To better understand and compare with our experimental findings, we also calculate the exciton binding energy using an electrostatic model as sketched in Figure 3, panel a.⁵² In the model, we approximate

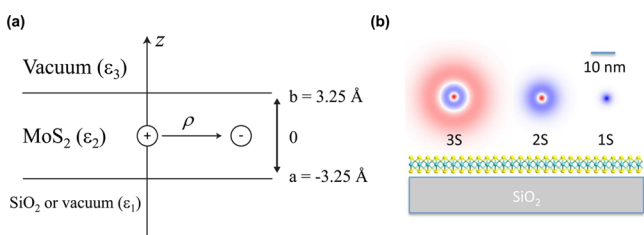


Figure 3. (a) An electrostatic model to calculate the exciton binding energy of monolayer MoS₂ on a SiO₂/Si substrate. (b) The calculated lowest few excitonic states, with corresponding binding energies of $E_{\text{ex}} = 280, 85,$ and 41 meV for the 1s, 2s, and 3s states, respectively. The scale bar is only used for the excitons shown in the schematic, while the TMD layer is exaggerated for the display purposes.

the system as three coplanar dielectric slabs: the MoS₂ monolayer, 6.5 Å thick with a static dielectric constant $\epsilon_2 = 14.5$, surrounded by either vacuum on both sides ($\epsilon_1 = \epsilon_2 = 1$) or vacuum and SiO₂ ($\epsilon_1 = 3.9, \epsilon_3 = 1$). Naturally, we confine the electron and hole to the middle of each MoS₂ monolayer. Using a field method described by Smythe⁵³ and extended by Sritharan,⁵⁴ we can calculate the potential experienced by an electron at (ρ, z) due to the presence of a hole at $(0, z_0)$ (see Supporting Information). The simulation yields binding energies of the lowest exciton (1s) of $E_{\text{ex}} = 280$ meV for a MoS₂ monolayer on SiO₂. The corresponding 1s exciton binding energy for a free-standing MoS₂ monolayer is $E_{\text{ex}} = 500$ meV. The 44% reduction of E_{ex} by considering a SiO₂ substrate explicitly demonstrates the sensitivity of E_{ex} to the screening from the dielectric environment.²² The experimentally determined exciton binding energy (230 meV) is in reasonable agreement with our model simulation (280 meV). Uncertainties that remain could largely be an effect of the imprecise determination of TIBB in our experiment. This simulation also yields the complete hydrogenic series of high lying excitons. Figure 3, panel b plots the lowest a few excitonic states, with corresponding binding energies of $E_{\text{ex}} = 280, 85,$ and 41 meV for the 1s, 2s, and 3s states, respectively. We note that our calculated binding energy of excitonic states does not follow the $1/n^2$ ($n =$ orbital angular momentum) rule expected in a hydrogenic Rydberg series. This is consistent with recent studies on monolayer WS₂⁵⁵ and is due to the nonuniform dielectric environment in 2D monolayer TMDs.

Finally, we discuss the grain boundaries of monolayer MoS₂. A grain boundary naturally forms when two grains are merged together during the growth of our polycrystalline MOCVD thin film. Figure 4, panel a is a large scan of sample surface showing

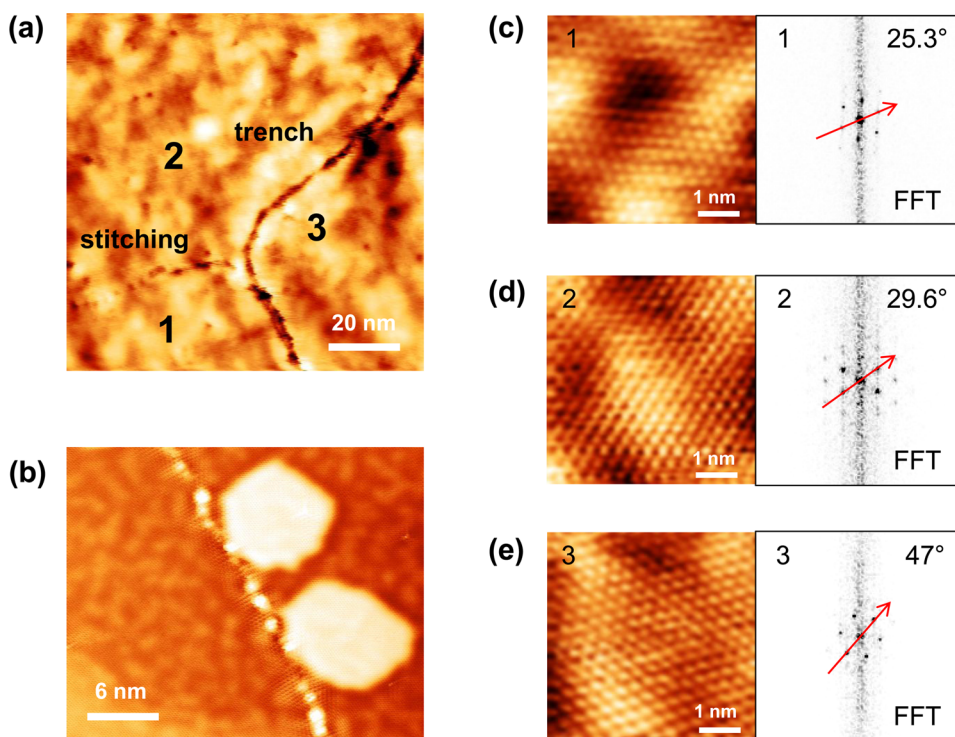


Figure 4. (a) A large STM image of MoS₂ showing a region with two types of grain boundaries, which separate the area into three domains as labeled by the numbers (set point: $V = 2.5$ V, $I = 20$ pA). (b) A grain boundary of CVD graphene grown on a copper substrate showing the presence of additional states at the grain boundary (set point: $V = 1$ V, $I = 100$ pA). (c–e) Atomically resolved STM images of MoS₂ for each domain in panel a and their Fourier transforms (set point: $V = 2$ V, $I = 50$ pA).

two types of grain boundaries. One boundary type shows a “trench” structure with a central dip, while the second one is characterized by a row of discrete spots reminiscent of “stitching”. These two grain boundaries separate the surface into three domains as labeled in Figure 4, panel a. We achieve atomic resolution for each domain (Figure 4c–e). These atomically resolved images and their Fourier transforms help us to determine the grain orientation and, hence, grain boundary misorientation angle. One can see that the “stitching” boundary is actually associated with a much smaller misorientation angle (4.3°) than that of “trench” boundary (21.7° and 17.4°). In our topographic images of the MoS₂ grain boundary, we see the boundary as largely featureless. This situation is to be contrasted with the case of grain boundaries in graphene grown by CVD techniques. Shown in Figure 4, panel b is a typical STM topographic image of a stitching grain boundary in graphene grown on copper foil. One sees a significant enhancement of the local density of states near the grain boundary of graphene indicating the presence of one or more edge states. Such states have also been seen before at the boundaries of graphene ribbons or sheets at low energies.^{56,57} The fact that the MoS₂ grain boundaries do not show a similar strong enhancement indicates that the contributions of such edge states to the overall local density of states are small. We note that other measurements²³ of CVD-grown MoS₂ on graphite substrates have shown density of states variations at grain boundaries. The nature of such edge states is highly dependent on the chemistry of the actual grain boundary, and our current findings are consistent with transport measurements on the same MOCVD samples that indicate that grain boundaries in MoS₂ do not scatter charge carriers strongly in these films.³⁷

In conclusion, we have provided an atomic-scale characterization of the structure and spectroscopic properties of monolayer MoS₂ grown by MOCVD techniques. Our measurements indicate that the atomic chemical defects in the film as grown by the MOCVD process are comparable in density to typical single-crystal samples of TMDs. Using a back-gated, insulating substrate allows us to conduct doping-dependent STS measurements on monolayer MoS₂. The gating dependence of the Fermi level indicates a large in-gap trap state density. Minimizing such traps will be of importance in electronic device performance. Our measurements of the band gap on the dielectric substrate together with PL measurements allow us to extract the exciton binding energies, consistent with simple theoretical estimates, and confirm the fact that Coulomb interactions are extremely strong in the excitonic state. The ability to do doping-dependent imaging and spectroscopy opens up several new avenues to study the unique physics of semiconducting monolayer TMDs and their heterostructures.^{58–61} Our experiments also lay the groundwork for future spectroscopic imaging measurements at lower temperatures to image localized quantum states and scattering in monolayer MoS₂.

■ ASSOCIATED CONTENT

■ Supporting Information

The Supporting Information is available free of charge on the ACS Publications website at DOI: 10.1021/acs.nanolett.6b00473.

STM topography of a step edge from monolayer to bilayer MoS₂, model calculations of tip-induced band

bending, an image potential calculation, and modeling of the exciton binding energy (PDF)

■ AUTHOR INFORMATION

Notes

The authors declare no competing financial interest.

■ ACKNOWLEDGMENTS

The STM sample preparation and characterization were supported by the Office of Naval Research (Award No. N00014-14-1-0501, A.D.), the National Science Foundation (NSF) MRSEC program through Columbia in the Center for Precision Assembly of Superstratic and Superatomic Solids (DMR-1420634, X.Z.), and the Air Force Office of Scientific Research (Award No. FA9550-11-1-0010, A.N.P.). Sample synthesis at Cornell was supported by the AFOSR (FA2386-13-1-4118) and the Nano Material Technology Development Program through the National Research Foundation of Korea (NRF) funded by the Ministry of Science, ICT, and Future Planning (2012M3A7B4049887). Additional funding for sample synthesis was provided by the NSF through the Cornell Center for Materials Research (NSF DMR-1120296).

■ REFERENCES

- (1) Radisavljevic, B.; Radenovic, A.; Brivio, J.; Giacometti, V.; Kis, A. *Nat. Nanotechnol.* **2011**, *6* (3), 147–150.
- (2) Mak, K. F.; Lee, C.; Hone, J.; Shan, J.; Heinz, T. F. *Phys. Rev. Lett.* **2010**, *105* (13), 136805.
- (3) Splendiani, A.; Sun, L.; Zhang, Y.; Li, T.; Kim, J.; Chim, C.-Y.; Galli, G.; Wang, F. *Nano Lett.* **2010**, *10* (4), 1271–1275.
- (4) Mak, K. F.; McGill, K. L.; Park, J.; McEuen, P. L. *Science* **2014**, *344* (6191), 1489–1492.
- (5) Xu, X.; Yao, W.; Xiao, D.; Heinz, T. F. *Nat. Phys.* **2014**, *10* (5), 343–350.
- (6) Zeng, H.; Dai, J.; Yao, W.; Xiao, D.; Cui, X. *Nat. Nanotechnol.* **2012**, *7* (8), 490–493.
- (7) Mak, K. F.; He, K.; Shan, J.; Heinz, T. F. *Nat. Nanotechnol.* **2012**, *7* (8), 494–498.
- (8) Mak, K. F.; He, K.; Lee, C.; Lee, G. H.; Hone, J.; Heinz, T. F.; Shan, J. *Nat. Mater.* **2012**, *12* (3), 207–211.
- (9) Cui, X.; Lee, G.-H.; Kim, Y. D.; Arefe, G.; Huang, P. Y.; Lee, C.-H.; Chenet, D. A.; Zhang, X.; Wang, L.; Ye, F.; Pizzocchero, F.; Jessen, B. S.; Watanabe, K.; Taniguchi, T.; Muller, D. A.; Low, T.; Kim, P.; Hone, J. *Nat. Nanotechnol.* **2015**, *10* (6), 534–540.
- (10) Radisavljevic, B.; Kis, A. *Nat. Mater.* **2013**, *12* (9), 815–820.
- (11) Costanzo, D.; Jo, S.; Berger, H.; Morpurgo, A. F. *Nat. Nanotechnol.* **2016**, *11*, 339.
- (12) Ross, J. S.; Wu, S.; Yu, H.; Ghimire, N. J.; Jones, A. M.; Aivazian, G.; Yan, J.; Mandrus, D. G.; Xiao, D.; Yao, W.; Xu, X. *Nat. Commun.* **2013**, *4*, 1474.
- (13) Seyler, K. L.; Schaibley, J. R.; Gong, P.; Rivera, P.; Jones, A. M.; Wu, S.; Yan, J.; Mandrus, D. G.; Yao, W.; Xu, X. *Nat. Nanotechnol.* **2015**, *10* (5), 407–411.
- (14) Chernikov, A.; van der Zande, A. M.; Hill, H. M.; Rigosi, A. F.; Velauthapillai, A.; Hone, J.; Heinz, T. F. *Phys. Rev. Lett.* **2015**, *115* (12), 126802.
- (15) Lee, C.; Yan, H.; Brus, L. E.; Heinz, T. F.; Hone, J.; Ryu, S. *ACS Nano* **2010**, *4* (5), 2695–2700.
- (16) Duerloo, K.-A. N.; Li, Y.; Reed, E. J. *Nat. Commun.* **2014**, *5*, 4214.
- (17) Koppera, R.; Voiry, D.; Yalcin, S. E.; Branch, B.; Gupta, G.; Mohite, A. D.; Chhowalla, M. *Nat. Mater.* **2014**, *13* (12), 1128–1134.
- (18) Jin, W.; Yeh, P.-C.; Zaki, N.; Zhang, D.; Sadowski, J. T.; Al-Mahboob, A.; van der Zande, A. M.; Chenet, D. A.; Dadap, J. I.; Herman, I. P.; Sutter, P.; Hone, J.; Osgood, R. M. *Phys. Rev. Lett.* **2013**, *111* (10), 106801.

- (19) Miwa, J. A.; Ulstrup, S.; Sørensen, S. G.; Dendzik, M.; Čabo, A. G.; Bianchi, M.; Lauritsen, J. V.; Hofmann, P. *Phys. Rev. Lett.* **2015**, *114* (4), 046802.
- (20) Zhang, C.; Johnson, A.; Hsu, C.-L.; Li, L.-J.; Shih, C.-K. *Nano Lett.* **2014**, *14* (5), 2443–2447.
- (21) Liu, H.; Jiao, L.; Yang, F.; Cai, Y.; Wu, X.; Ho, W.; Gao, C.; Jia, J.; Wang, N.; Fan, H.; Yao, W.; Xie, M. *Phys. Rev. Lett.* **2014**, *113* (6), 066105.
- (22) Ugeda, M. M.; Bradley, A. J.; Shi, S.-F.; da Jornada, F. H.; Zhang, Y.; Qiu, D. Y.; Ruan, W.; Mo, S.-K.; Hussain, Z.; Shen, Z.-X.; Wang, F.; Louie, S. G.; Crommie, M. F. *Nat. Mater.* **2014**, *13* (12), 1091–1095.
- (23) Huang, Y. L.; Chen, Y.; Zhang, W.; Quek, S. Y.; Chen, C.-H.; Li, L.-J.; Hsu, W.-T.; Chang, W.-H.; Zheng, Y. J.; Chen, W.; Wee, A. T. S. *Nat. Commun.* **2015**, *6*, 6298.
- (24) Bradley, A. J.; Ugeda, M.; da Jornada, F. H.; Qiu, D. Y.; Ruan, W.; Zhang, Y.; Wickenburg, S.; Riss, A.; Lu, J.; Mo, S.-K.; Hussain, Z.; Shen, Z.-X.; Louie, S. G.; Crommie, M. F. *Nano Lett.* **2015**, *15* (4), 2594–2599.
- (25) Yankowitz, M.; McKenzie, D.; LeRoy, B. J. *Phys. Rev. Lett.* **2015**, *115* (13), 136803.
- (26) Allain, A.; Kang, J.; Banerjee, K.; Kis, A. *Nat. Mater.* **2015**, *14* (12), 1195–1205.
- (27) Lu, C.-P.; Li, G.; Mao, J.; Wang, L.-M.; Andrei, E. Y. *Nano Lett.* **2014**, *14* (8), 4628–4633.
- (28) Zhang, Y.; Brar, V. W.; Girit, C.; Zettl, A.; Crommie, M. F. *Nat. Phys.* **2009**, *5* (10), 722–726.
- (29) Xue, J.; Sanchez-Yamagishi, J.; Bulmash, D.; Jacquod, P.; Deshpande, A.; Watanabe, K.; Taniguchi, T.; Jarillo-Herrero, P.; LeRoy, B. J. *Nat. Mater.* **2011**, *10* (4), 282–285.
- (30) Brar, V. W.; Wickenburg, S.; Panlasigui, M.; Park, C.-H.; Wehling, T. O.; Zhang, Y.; Decker, R.; Girit, C.; Balatsky, A. V.; Louie, S. G.; Zettl, A.; Crommie, M. F. *Phys. Rev. Lett.* **2010**, *104* (3), 036805.
- (31) Zhang, Y.; Brar, V. W.; Wang, F.; Girit, C.; Yayon, Y.; Panlasigui, M.; Zettl, A.; Crommie, M. F. *Nat. Phys.* **2008**, *4* (8), 627–630.
- (32) Wang, Y.; Wong, D.; Shytov, A. V.; Brar, V. W.; Choi, S.; Wu, Q.; Tsai, H.-Z.; Regan, W.; Zettl, A.; Kawakami, R. K.; Louie, S. G.; Levitov, L. S.; Crommie, M. F. *Science* **2013**, *340* (6133), 734–737.
- (33) Brar, V. W.; Decker, R.; Solowan, H.-M.; Wang, Y.; Maserati, L.; Chan, K. T.; Lee, H.; Girit, C. O.; Zettl, A.; Louie, S. G.; Cohen, M. L.; Crommie, M. F. *Nat. Phys.* **2011**, *7* (1), 43–47.
- (34) Lee, Y. H.; Zhang, X. Q.; Zhang, W.; Chang, M. T.; Lin, C. T.; Chang, K. D.; Yu, Y. C.; Wang, J. T. W.; Chang, C. S.; Li, L. J.; Lin, T.-W. *Adv. Mater.* **2012**, *24* (17), 2320–2325.
- (35) Najmaei, S.; Liu, Z.; Zhou, W.; Zou, X.; Shi, G.; Lei, S.; Yakobson, B. I.; Idrobo, J.-C.; Ajayan, P. M.; Lou, J. *Nat. Mater.* **2013**, *12* (8), 754–759.
- (36) van der Zande, A. M.; Huang, P. Y.; Chenet, D. A.; Berkelbach, T. C.; You, Y.; Lee, G.-H.; Heinz, T. F.; Reichman, D. R.; Muller, D. A.; Hone, J. C. *Nat. Mater.* **2013**, *12* (6), 554–561.
- (37) Kang, K.; Xie, S.; Huang, L.; Han, Y.; Huang, P. Y.; Mak, K. F.; Kim, C.-J.; Muller, D.; Park, J. *Nature* **2015**, *520* (7549), 656–660.
- (38) Liu, H.; Si, M.; Deng, Y.; Neal, A. T.; Du, Y.; Najmaei, S.; Ajayan, P. M.; Lou, J.; Ye, P. D. *ACS Nano* **2014**, *8* (1), 1031–1038.
- (39) Lauffer, P.; Emtsev, K.; Graupner, R.; Seyller, T.; Ley, L.; Reshanov, S.; Weber, H. *Phys. Rev. B: Condens. Matter Mater. Phys.* **2008**, *77* (15), 155426.
- (40) Tersoff, J.; Hamann, D. R. *Phys. Rev. B: Condens. Matter Mater. Phys.* **1985**, *31* (2), 805–813.
- (41) Popov, I.; Seifert, G.; Tománek, D. *Phys. Rev. Lett.* **2012**, *108* (15), 156802.
- (42) Choi, S.; Shaolin, Z.; Yang, W. J. *Korean Phys. Soc.* **2014**, *64* (10), 1550–1555.
- (43) Cheiwchanchamnangij, T.; Lambrecht, W. R. L. *Phys. Rev. B: Condens. Matter Mater. Phys.* **2012**, *85* (20), 205302.
- (44) Zhang, C.; Chen, Y.; Johnson, A.; Li, M.-Y.; Li, L.-J.; Mende, P. C.; Feenstra, R. M.; Shih, C.-K. *Nano Lett.* **2015**, *15* (10), 6494–6500.
- (45) Feenstra, R. M.; Stroscio, J. A. *J. Vac. Sci. Technol., B: Microelectron. Process. Phenom.* **1987**, *5* (4), 923–929.
- (46) McEllistrem, M.; Haase, G.; Chen, D.; Hamers, R. *Phys. Rev. Lett.* **1993**, *70* (16), 2471.
- (47) Feenstra, R. M.; Dong, Y.; Semtsiv, M.; Masselink, W. *Nanotechnology* **2007**, *18* (4), 044015.
- (48) Neaton, J. B.; Hybertsen, M. S.; Louie, S. G. *Phys. Rev. Lett.* **2006**, *97* (21), 216405.
- (49) Lin, H.; Lagoute, J.; Repain, V.; Chacon, C.; Girard, Y.; Lauret, J.-S.; Ducastelle, F.; Loiseau, A.; Rousset, S. *Nat. Mater.* **2010**, *9* (3), 235–238.
- (50) Ramasubramaniam, A. *Phys. Rev. B: Condens. Matter Mater. Phys.* **2012**, *86* (11), 115409.
- (51) Komsa, H.-P.; Krasheninnikov, A. V. *Phys. Rev. B: Condens. Matter Mater. Phys.* **2012**, *86* (24), 241201.
- (52) Zhu, X.; Monahan, N. R.; Gong, Z.; Zhu, H.; Williams, K. W.; Nelson, C. A. *J. Am. Chem. Soc.* **2015**, *137* (26), 8313–8320.
- (53) Smythe, W. R. *Static and Dynamic Electricity*; McGraw-Hill: New York, 1950; Vol. 3.
- (54) Sritharan, S. *arXiv:1312.7392* **2013**.
- (55) Chernikov, A.; Berkelbach, T. C.; Hill, H. M.; Rigosi, A.; Li, Y.; Aslan, O. B.; Reichman, D. R.; Hybertsen, M. S.; Heinz, T. F. *Phys. Rev. Lett.* **2014**, *113* (7), 076802.
- (56) Tao, C.; Jiao, L.; Yazyev, O. V.; Chen, Y.-C.; Feng, J.; Zhang, X.; Capaz, R. B.; Tour, J. M.; Zettl, A.; Louie, S. G.; Dai, H.; Crommie, M. F. *Nat. Phys.* **2011**, *7* (8), 616–620.
- (57) Park, J.; Lee, J.; Liu, L.; Clark, K. W.; Durand, C.; Park, C.; Sumpter, B. G.; Baddorf, A. P.; Mohsin, A.; Yoon, M.; Gu, G.; Li, A.-P. *Nat. Commun.* **2014**, *5*, 5403.
- (58) Liang, Y.; Yang, L. *Phys. Rev. Lett.* **2015**, *114* (6), 063001.
- (59) Ramasubramaniam, A.; Naveh, D.; Towe, E. *Phys. Rev. B: Condens. Matter Mater. Phys.* **2011**, *84* (20), 205325.
- (60) Riley, J. M.; Meevasana, W.; Bawden, L.; Asakawa, M.; Takayama, T.; Eknapakul, T.; Kim, T. K.; Hoesch, M.; Mo, S. K.; Takagi, H.; Sasagawa, T.; Bahramy, M. S.; King, P. D. C. *Nat. Nanotechnol.* **2015**, *10* (12), 1043–1047.
- (61) Larentis, S.; Tolsma, J. R.; Fallahzad, B.; Dillen, D. C.; Kim, K.; MacDonald, A. H.; Tutuc, E. *Nano Lett.* **2014**, *14* (4), 2039–2045.